Origin of Pyroelectricity in Ferroelectric HfO$_2$

J. Liu,[1,2,*] S. Liu,[3,4,†] L. H. Liu,[1] B. Hanrahan,[3] and S. T. Pantelides[2,5]

[1]*Optics and Thermal Radiation Research Center, Shandong University, Qingdao, Shandong 266237, China*

[2]*Department of Physics and Astronomy, Vanderbilt University, Nashville, Tennessee 37235, USA*

[3]*Sensors & Electron Devices Directorate, U.S. Army Research Laboratory, Adelphi, Maryland 20783, USA*

[4]*School of Science, Westlake University, Hangzhou, Zhejiang 310024, China*

[5]*Department of Electrical Engineering and Computer Science, Vanderbilt University, Nashville, Tennessee 37235, USA*

The pyroelectric response of materials is a promising phenomenon that is used in many applications. Here, we report first-principles lattice dynamics and *ab initio* molecular dynamics calculations to investigate the mechanisms of the pyroelectric effect in the *Pca2$_1$* orthorhombic phase of HfO$_2$; this is an emerging pyroelectric material with promising technological applications. With first-principles lattice dynamics calculations, we demonstrate a large pyroelectric response that is intrinsic to the pure *Pca2$_1$* orthorhombic phase. Unlike most conventional ferroelectric pyroelectrics, such large pyroelectricity arises unexpectedly from the secondary effect (induced by the negative longitudinal piezoelectric effect) that has not received due attention. *Ab initio* molecular dynamics simulations further demonstrate a giant pyroelectric response that is associated with an orthorhombic (polar) to tetragonal (nonpolar) structural phase transition. Upon the incorporation of Si dopants with increasing dopant concentrations, the phase transition persists, but occurs at reduced temperatures with enhanced pyroelectric responses. The present work highlights the importance of the secondary pyroelectric effect responsible for the pyroelectricity in HfO$_2$ and its promising potential for device applications.

I. INTRODUCTION

All ferroelectrics carry a spontaneous polarization that varies with temperature [1,2]. The change in polarization resulting from a temperature variation generates a voltage, which is known as pyroelectricity [1,2]. Thus, all ferroelectrics are pyroelectric, but the inverse is not necessarily true. The pyroelectric response is the key property responsible for a wide range of applications, such as thermal imaging [2,3] and pyroelectric energy harvesting [4,5]. Despite the fundamental interest and the concomitant technological importance, first-principles investigations of the pyroelectric effect have not received due attention. As a result, a satisfactory understanding of the pyroelectric effect is still lacking, especially for new pyroelectric materials. For example, an unusually large secondary pyroelectricity (associated with piezoelectricity and thermal expansion) has recently been demonstrated in group-IV monochalcogenide monolayers [6–9], contrary to the general belief that the secondary effect plays a minor role in bulk pyroelectrics [2].

*jian.liu@alumni.stonybrook.edu
†liushi@westlake.edu.cn

The recent discovery of unexpected ferroelectricity (and hence, pyroelectricity) in both pure and doped hafnia (HfO$_2$) thin films [10,11] combined with their great complementary metal oxide semiconductor (CMOS) compatibility make hafnia a promising candidate for nanoscale device applications, such as pyroelectric energy harvesting and infrared detection [12–14]. While it has been theoretically demonstrated that Si doping promotes the stabilization of the orthorhombic phase of HfO$_2$ [15,16], doping [12,17] and alloying [18] can also tune the pyroelectric response of HfO$_2$-based pyroelectrics. Large pyroelectric response has been observed in Si-doped HfO$_2$ thin films; this is attributed to the temperature- and field-induced orthorhombic (polar) to tetragonal (nonpolar) transition [12]. Very recently, scattered data of pyroelectric coefficients that vary with dopant concentration, film thickness, and wake-up cycles have been reported for Si-doped HfO$_2$ [12,17,19–21]. Further development and optimization of HfO$_2$-based pyroelectric devices require a detailed quantitative understanding of the nature of the pyroelectricity in ferroelectric HfO$_2$. Reliable interatomic potentials are still lacking for HfO$_2$, preventing large-scale finite-temperature MD simulations.

In the first part of this paper, we use the recently developed first-principles lattice-dynamics approach to identify the underlying mechanisms responsible for the pyroelectric effect in pure ferroelectric HfO_2, at temperatures below the ferroelectric to paraelectric transition. Unlike in most conventional ferroelectric pyroelectrics, we demonstrate a large and dominating secondary pyroelectric response in the $Pca2_1$ orthorhombic phase of HfO_2, which is induced by a significant negative longitudinal piezoelectricity together with an isotropic positive thermal expansion. In the second part of this paper, we perform *ab initio* molecular dynamics simulations to further demonstrate that the secondary effect is associated with an orthorhombic (polar) to tetragonal (nonpolar) structural phase transition at around 850 K. The transition "pathway" involves translational displacements of Hf and O sublattices towards their centrosymmetric positions, and no order–disorder character is identified. Furthermore, the phase transition persists with the incorporation of Si dopants. With increasing dopant concentrations, the transition temperature is reduced and the primary pyroelectric response is enhanced because substitutional Si doping perturbs the local chemical environment, which introduces strong anharmonicity to the host HfO_2 structure. The present work unravels the secondary pyroelectric effect that is responsible for the pyroelectricity in HfO_2 and offers important implications for practical energy and sensor applications utilizing HfO_2-based pyroelectrics.

II. THEORY

At temperatures below the ferroelectric to paraelectric phase-transition temperature, pyroelectricity [22] (defined as the response of the spontaneous polarization, P_s, with respect to fluctuations in temperature, T) at constant stress, σ, is conventionally separated into two parts [2,23,24]: the primary (at constant external strain, ε), $\Pi_1(T)$, and the secondary, $\Pi_2(T)$:

$$\Pi = \left(\frac{dP_S}{dT}\right)_\sigma = \left(\frac{\partial P_S}{\partial T}\right)_\varepsilon + \sum_i \left(\frac{\partial P_S}{\partial \varepsilon_i}\right)_T \left(\frac{\partial \varepsilon_i}{\partial T}\right)_\sigma. \quad (1)$$

The secondary part, $\Pi_2(T)$, accounts for the pyroelectricity that is associated with piezoelectricity and thermal expansion. It can be readily obtained from the piezoelectric stress constants, e ($\partial P_S/\partial \varepsilon_i$), and the thermal expansion coefficients, α ($\partial \varepsilon_i/\partial T$), and is generally much smaller than the primary part for conventional ferroelectrics [2]. The primary part, $\Pi_1(T)$, on the other hand, accounts for the "clamped-lattice" pyroelectricity. With the fixed lattice parameters, the internal structural parameters vary with temperature (referred to as "internal" thermal expansion in this paper, by analogy with "thermal expansion", which

describes the variation of lattice parameters with temperature). The change of P_S with respect to atomic displacements, ($\partial P_S/\partial Q_{\bar{0}j}$), defines Born effective charges (BEC), Z^* [25]. It is then clear that part of primary pyroelectricity arises because the lattice exhibits "internal thermal expansion" while ions carry rigid BECs. This picture is usually referred to as the point-charge or rigid-ion model [26,27], as the renormalization of BECs due to electron-phonon interactions is neglected. The corresponding rigid-ion primary pyroelectricity reads [6,28]

$$\left(\frac{\partial P_S}{\partial T}\right)_\varepsilon = \sum_j \left(\frac{\partial P_S}{\partial Q_{\bar{0}j}}\right)_T \left(\frac{\partial Q_{\bar{0}j}}{\partial T}\right)_\varepsilon, \quad (2)$$

where the Q is the normal-mode amplitude, and the summation, j, runs over $\vec{q} = 0$ optical modes of symmetries, which allow nonvanishing contributions ($\langle Q_{\bar{0}j}\rangle \neq 0$). $\langle Q_{\bar{0}j}\rangle$ is calculated with the quasi-harmonic approximation [6,28]

$$\langle Q_{\bar{0}j}\rangle = -\sum_{\vec{q}\lambda} \frac{\hbar}{2} \frac{2n_{\vec{q}\lambda} + 1}{\omega_{\bar{0}j}^2} \frac{\partial \omega_{\vec{q}\lambda}}{\partial Q_{\bar{0}j}}, \quad (3)$$

where ω are the phonon eigenfrequencies of mode λ at wavevector $\vec{q}$, and n is the Bose-Einstein distribution function.

III. METHODS

Density functional theory (DFT) total energy and density functional perturbation theory (DFPT) lattice dynamics calculations [29] have been performed using the QUANTUM ESPRESSO package [30]. Spontaneous polarization is calculated using the modern theory of polarization (Berry-phase method) [25,31–33]. For electronic-structure calculations, we use the local density approximation (LDA) [34,35] to describe the exchange-correlation functional. Ultrasoft pseudopotentials are taken from the PSLibrary [36]. The electronic wave functions are expanded in a plane-wave basis with a kinetic energy cutoff of 140 Ry. For Brillouin-zone sampling, a $4 \times 4 \times 4$ k-point mesh is used. Phonons are calculated on the same q-point mesh. All structures given in figures are produced using VESTA [37]. In Eq. (3), to compute $\partial \omega_{\vec{q}\lambda}/\partial Q_{\bar{0}j}$, a central difference scheme is used through displacing atoms in the unit cell collectively by $Q_{\bar{0}j}$. Details of the first-principles lattice dynamics method can be found in Ref. [28].

Ab initio molecular dynamics (AIMD) simulations are performed using a basis of linear combinations of localized atomic orbitals, as implemented in the SIESTA package [38]. The $Pca2_1$ orthorhombic phase of HfO_2 is modeled by a supercell of 324 atoms ($3 \times 3 \times 3$ unit cells). To model Si-doped HfO_2, 2 and 4 Hf atoms are replaced by Si atoms, corresponding to substitutional doping concentrations of 1.85 and 3.7 cat.% (0.62 and 1.23 at.%)

respectively. A variationally optimized double-ζ polarized basis set is used with a mesh cutoff of 250 Ry for the real-space grid. Temperature is raised sequentially, i.e., the initial position and velocity of the simulation at a higher temperature are generated from the final snapshot of the simulation at a lower temperature. For each AIMD simulation, a trajectory of 0.5 ps is used for production after an equilibration stage of 0.5 ps, with a time step of 1 fs. To highlight the secondary pyroelectric effect, simulations are performed within the *NVT* and *NPT* ensembles, with temperature and pressure controlled by a Nosé thermostat [39] and Parrinello-Rahman barostat [40], respectively. Spontaneous polarization is evaluated for the ensemble-averaged structure at each temperature.

The pyroelectric coefficient is determined for a 5 at.% Al-doped HfO$_2$ thin film, in a manner similar to Refs. [41,42]. The film is grown on 100-nm-thick reactively sputtered TiN on a silicon substrate. The atomic layer deposition (ALD) process uses metal organic precursors, tetrakis(ethylmethylamino)hafnium (TEMAH) and trimethylaluminum (TMA), for the cations and ozone is used as the oxidant with argon as a carrier gas. The Al$_2$O$_3$ content is defined by using a 1:19 cycle ratio. The total film thickness of 20 nm is achieved by altering the number of supercycles, which are monitored *in situ* through ellipsometry. A TiN top electrode is reactively sputtered then defined using the RCA-1 etch. Samples are annealed at 700 °C for 20 s in an N$_2$ environment. The pyroelectric coefficient is determined by oscillating the temperature of a TiN/Al-HfO$_2$/TiN capacitor and measuring the generated current. To determine the sample temperature, a calibrated resistive thermal device chip is colocated on a hotplate with the Al-HfO$_2$ capacitor. The temperature

and current profiles are used to determine the pyroelectric coefficient, Π

$$I_p = \Pi A \frac{dT}{dt}, \qquad (4)$$

where I_p is the pyroelectric current, A is the capacitor area, and dT/dt is the temperature rate of change. See detailed experimental setups in Refs. [41,42].

IV. RESULTS

Hafnia (HfO$_2$) in the bulk state is nonpolar, as its room-temperature monoclinic $P2_1/c$ phase is centrosymmetric [43]. A consensus has seemingly been reached that the origin of the unexpected ferroelectricity in thin-film HfO$_2$ is due to the $Pca2_1$ orthorhombic phase probably being stabilized by a variety of extrinsic factors, such as residual stresses, dopants, oxygen vacancies, and the surface effect in small grains [10,11,44–48]. Ferroelectricity has also been observed in undoped thin films of HfO$_2$ [49]. The polar $Pca2_1$ orthorhombic phase and associated nonpolar $P4_2/nmc$ tetragonal phase are both dynamically stable; the latter corresponds to a very shallow minimum of the energy landscape [43]. Our calculated lattice parameters for a, b, and c are 5.13, 4.92, and 4.95 Å, respectively, while the computed spontaneous polarization is 56 μC/cm^2 (taking the $P4_2/nmc$ tetragonal phase as the reference); this is in line with previous theoretical results based on a different exchange-correlation functional [43].

We first apply the lattice-dynamics approach to study the pyroelectricity in the pure $Pca2_1$ orthorhombic phase of HfO$_2$ (referred to as pure HfO$_2$ hereafter). The calculated room-temperature "intrinsic" (dopant-free and strain-free)
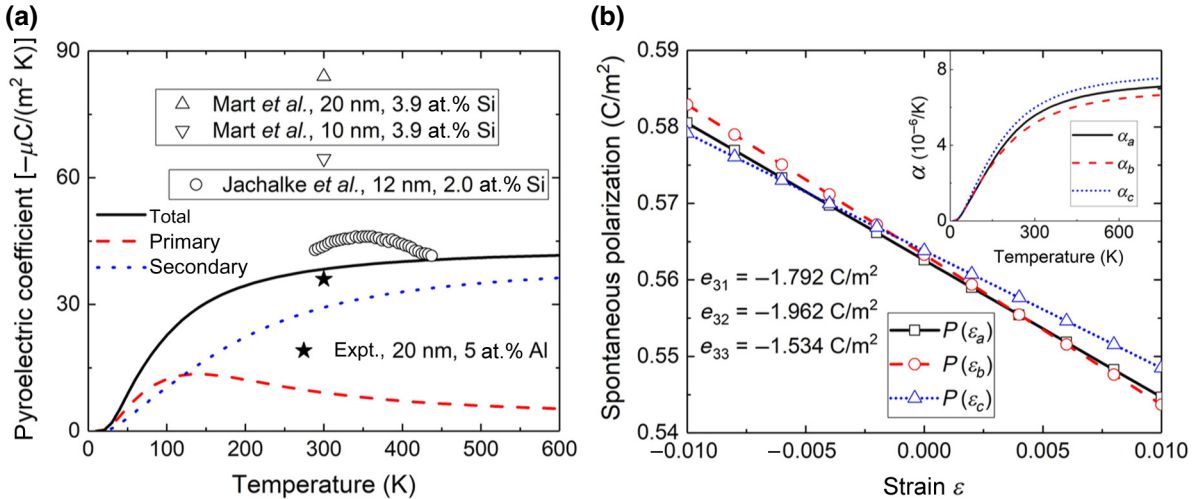

FIG. 1.   For the pure $Pca2_1$ orthorhombic phase of HfO$_2$: (a) Calculated primary and secondary pyroelectric coefficients, compared with experimental data for thin films of Al-doped (this work) and Si-doped (maximum values in each experiment) HfO$_2$. (b) Calculated piezoelectric (main panel) and thermal expansion (inset) components in the secondary pyroelectric effect. Note that e_{33} is negative, i.e., pure HfO$_2$ exhibits negative longitudinal piezoelectricity.

Π is -38 μC/(m^2 K), which is smaller in magnitude than the maximum values of Π reported for Si-doped HfO$_2$ [17,19,20] (Π varies with dopant concentration and film thickness), while our measurement for a thin film of Al-doped HfO$_2$ is -36 μC/(m^2 K), as shown in Fig. 1(a). These results demonstrate that the pyroelectric effect observed in Si-doped HfO$_2$ can be largely accounted for by its "intrinsic" pyroelectricity. We will discuss the effects of Si doping shortly. In most conventional ferroelectric pyroelectrics, the primary pyroelectricity dominates the pyroelectric effect [2]. Surprisingly, in pure HfO$_2$, the secondary pyroelectricity dominates, as shown in Fig. 1(a).

Understanding the underlying mechanism responsible for such an intriguing pyroelectric response is of great importance for further improvement of future pyroelectric applications. In conventional ferroelectrics, such as PbTiO$_3$ [50], and nonferroelectrics, such as wurtzite semiconductors [25], the piezoelectric coefficients along the polar axis (e_{33}) and in the basal plane (e_{31}) are positive and negative, respectively, i.e., these materials exhibit "normal" piezoelectricity. One often-mentioned exception is the case of the ferroelectric polymer poly(vinylidene fluoride) (PVDF), in which e_{33} is negative [51]. More recently, such an unusual negative longitudinal piezoelectric effect was also found in several hexagonal *ABC* ferroelectrics [52]. We have found significant negative longitudinal piezoelectricity in pure HfO$_2$, as shown in Fig. 1(b). Considering the isotropic positive thermal expansion [see the inset of Fig. 1(b)], this results in a significant secondary pyroelectric effect ($\Pi_2 = \sum_j e_{cj}\alpha_j$; c is the polar axis). Note that significant secondary pyroelectricity could also arise in a different way, e.g., in the cases of PbTiO$_3$ and

group-IV monochalcogenide monolayers [7], which show "normal" piezoelectricity, but anisotropic thermal expansion (the two lattice constants along and perpendicular to the polar axis become shorter and longer with increasing temperatures, respectively).

The primary pyroelectricity, on the other hand, is intimately related to the anharmonicity of the lattice. In line with the fact that the paraelectric $P4_2/nmc$ tetragonal phase is dynamically stable (not a saddle point on the potential energy surface), the absence of a polar soft phonon mode is indicative of insignificant rigid-ion primary pyroelectricity. The eight zone-center phonon modes with A$_1$-TO symmetry responsible for the rigid-ion primary pyroelectricity (due to their nonvanishing mean normal-mode amplitudes, $Q_{\bar{0}j}$) are shown in Fig. 2. These phonon modes are only slightly anharmonic, as manifested in the almost parabolic shape of the energy landscape (calculated with ions statically displaced over a range of "frozen-in" normal-mode amplitudes). As a result, their contributions to $\Pi_1(T)$ are relatively insignificant (see Fig. S1 in the Supplemental Material [53]).

We have demonstrated that the large pyroelectric response (comparable to that of many commercially used pyroelectrics) is an intrinsic property of pure HfO$_2$, and arises unexpectedly from the secondary pyroelectric effect. To further demonstrate the secondary pyroelectric effect, we have performed AIMD simulations within the *NVT* and *NPT* ensembles, where thermal expansion is forbidden and allowed, respectively. The comparison is shown in the top panel of Fig. 3(a). In the *NVT* simulations, only the primary pyroelectric effect is included. An insignificant primary pyroelectricity is observed, as reflected by the
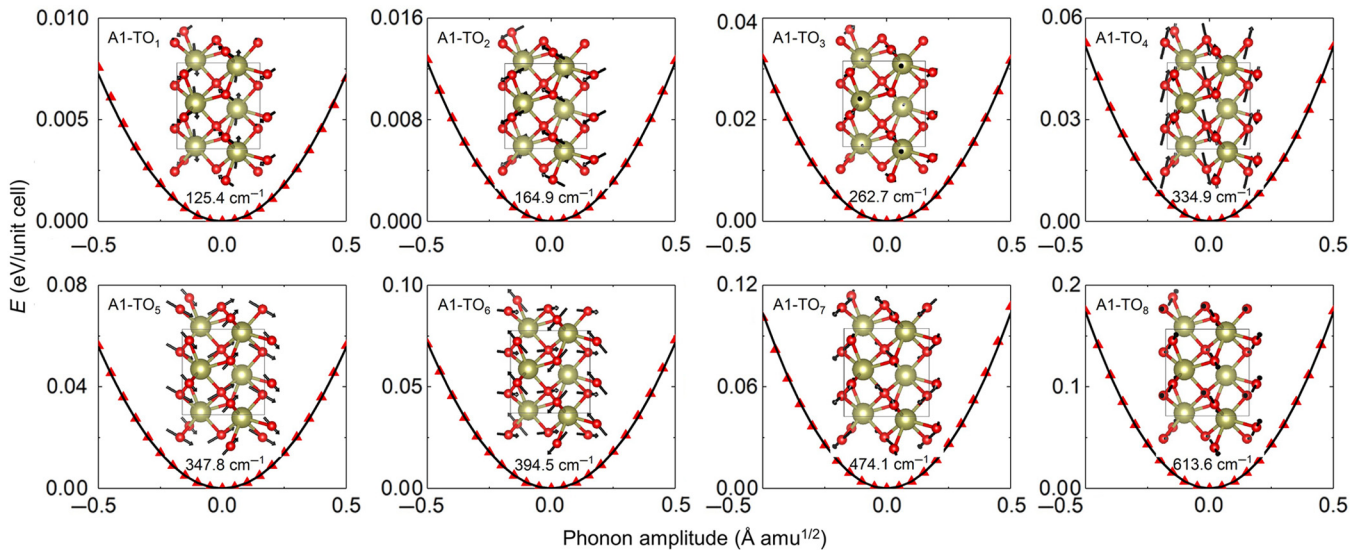

FIG. 2.   Zone-center TO phonon modes with A$_1$ symmetry. The arrows attached on the ions (Hf in gold, and O in red) indicate the eigenvector. Energies (triangles) are calculated with ions statically displaced over a range of "frozen-in" normal-mode amplitudes. The fitted harmonic potentials are shown by curves, while the legends indicate the corresponding eigenfrequencies.
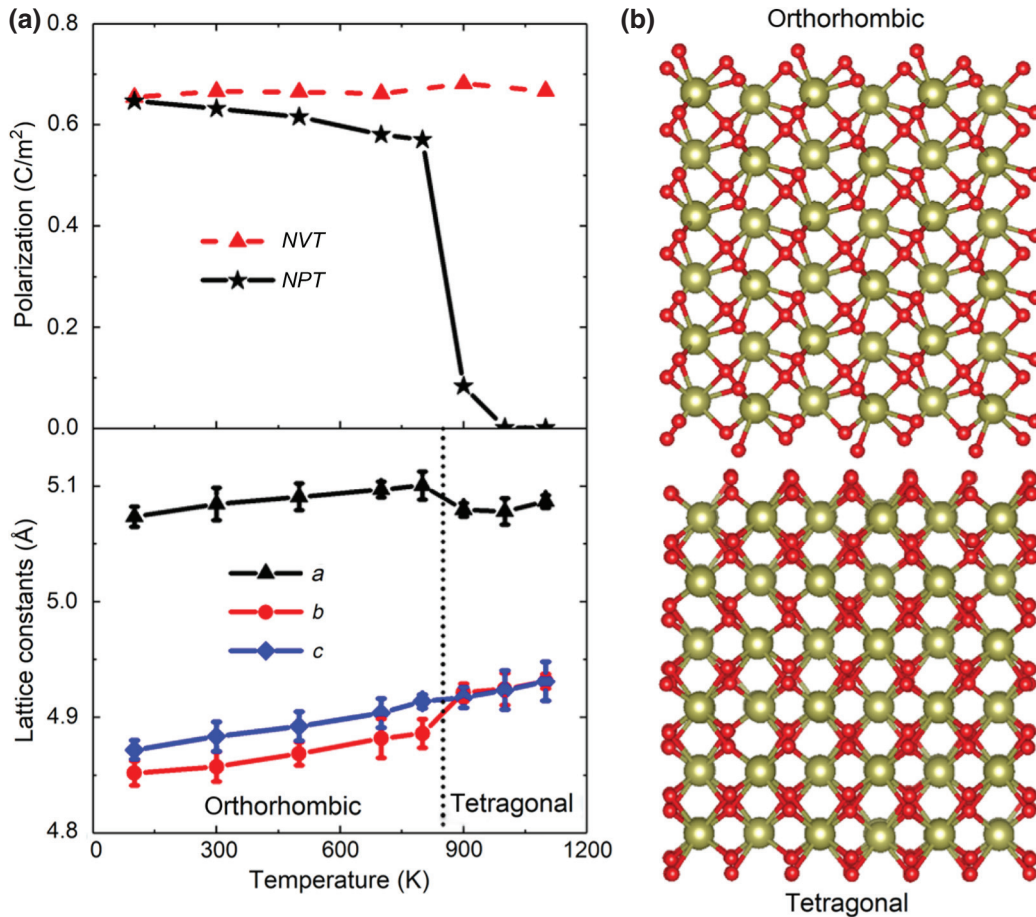
FIG. 3. (a) Top panel: pyroelectric response calculated with AIMD simulations. Bottom panel: temperature-dependent lattice constants calculated in the *NPT* simulations. The orthorhombic to tetragonal transition occurs at around 850 K, before and after which the two phases exhibit normal thermal expansion behavior. (b) Mean (ensemble-averaged) structures of the orthorhombic and tetragonal phases evaluated at 300 and 1100 K, respectively.

temperature-independent spontaneous polarization, which is consistent with our lattice-dynamics calculations. The small discrepancy is possibly due to the rather weak anharmonic nature of the corresponding phonon modes, and the limited time- and length-scales achievable by AIMD simulations. In the *NPT* simulations, the secondary pyroelectric effect is included as well. A large pyroelectric response is found; this is highlighted by the largely "isotropic" thermal expansion (the values of a, b, and c all increase with increasing temperature).

More importantly, there is a temperature-driven structural phase transition, after which the two lattice parameters b and c become equal, as shown in the bottom panel of Fig. 3(a). Such an orthorhombic (polar) to tetragonal (nonpolar) transition [see Fig. 3(b), and the Supplemental Material [52] for an AIMD movie at the transition] is in agreement with the experimental observations for a thin film of Si-doped HfO$_2$ [12,17]. The calculated transition temperature, T_c, for pure HfO$_2$ is around 850 K (750 K using the Perdew-Burke-Ernzerhof (PBE) functional [54],

as shown in Fig. S2 within the Supplemental Material [53]; this demonstrates that the phase-transition behavior is not substantially sensitive to the choice of density functional). It is noted that the exact value of T_c may be dependent on the size of the supercell. However, an accurate determination of T_c is beyond the scope of this work. The calculated T_c is higher than those reported for Si-doped HfO$_2$, which vary with dopant concentration and film thickness [12,17]; this suggests that the orthorhombic to tetragonal transition is an intrinsic property of pure HfO$_2$, i.e., the phase transition is not necessarily induced by the incorporation of Si dopants. The peak pyroelectric response near the transition is estimated roughly to be as large as -2400 μC/(m^2 K), comparable to the pyroelectric response of up to -1300 μC/(m^2 K) (Si-doped HfO$_2$, 9 nm, 5.6 at.%) reported by Hoffmann *et al.* [12].

The orthorhombic to tetragonal transition is found to exhibit a notable displacive character, as shown in Fig. 4(a). To demonstrate this, we define a parameter δ

as the relative distance (in fraction of lattice constant c) between the O and Hf planes in the polar direction [see the inset of Fig. 4(a)]. The probability distribution of δ exhibits a single peak at each temperature. With increasing temperatures, the peak broadens and shifts to the value of 0.25 that corresponds to the centrosymmetric positions along the polar direction. In our AIMD simulations, the transition occurs at around 850 K. To highlight the transition "pathway", the instantaneous unit-cell structures (projected from the supercell structures) during the transition are shown in Fig. 4(b). The transition "pathway" involves translational displacements of Hf and O sublattices towards their centrosymmetric positions (see the arrows in the upper-left panel of Fig. 4(b) and the animated movie of the orthorhombic to tetragonal transition in the Supplemental Material [52]). This displacement pattern is possibly indicative of a soft-mode-like behavior near the transition that is otherwise absent in the (zero-temperature) metastable tetragonal phase of HfO_2. Note that, within the time- and length-scales achieved by AIMD simulations, we are unable to identify any order–disorder character in the orthorhombic to tetragonal transition.

Last, but not least, we investigate the effects of Si doping on the pyroelectric response of orthorhombic HfO_2, for which seemingly contradictory experimental results were reported very recently [12,17,19]. Upon the incorporation of Si dopants with increasing dopant concentrations, we find that the aforementioned orthorhombic to tetragonal transition persists, but occurs at reduced temperatures, as shown in Fig. 5(a). As a result, the pyroelectric coefficients increase in magnitude with increasing dopant concentrations. This tendency is in remarkable agreement with the experimental observations found for a thin film of Si-doped HfO_2 [12,17]. For example, Hoffmann *et al.* [12] obtained pyroelectric coefficients of -950, -1100, and -1300 $\mu C/(m^2\,K)$ for 3.8, 4.3, and 5.6 at.% Si-doped HfO_2, while the phase-transition temperatures (at which the remanent polarization is reduced by half) are estimated to be 410, 330, and 170 K, respectively. Also, it can be

expected that the pyroelectric behavior eventually vanishes with further increasing the Si dopant concentrations, as observed in experiments [17,19].

Unlike the case of pure HfO_2, we find that the enhanced pyroelectric response for Si-doped HfO_2 arises mainly from the primary pyroelectric effect. Note that the two key components to determine the primary pyroelectricity are the atomic displacements of ions and the BECs they carry. While Si and Hf ions are equivalent (in the sense that they carry similar BECs), their local coordination environments are fundamentally different [16]. Hence, the incorporation of Si dopants perturbs the host HfO_2 structure and introduces strong anharmonicity (in particular, along the polar direction, see Fig. S3 within the Supplemental Material [53]), resulting in notable atomic displacements (and hence, primary pyroelectricity), as shown in Fig. 5(b). We further corroborate this conclusion by noting that piezoelectricity and thermal expansion of the lattice, i.e., the two key components that determine the secondary pyroelectricity, do not vary with Si dopant concentrations, as shown in Fig. S4 within the Supplemental Material [53]. Note also that the negative longitudinal piezoelectric effect found in pure HfO_2 persists in Si-doped HfO_2.

V. DISCUSSION

The pyroelectric response determines the performance of a material in various device applications, such as thermal infrared sensors and pyroelectric energy harvesters. The above theoretical investigations have demonstrated large intrinsic (the material is free to expand thermally) secondary pyroelectricity in HfO_2. This feature suggests that straining the lattice might have a significant impact on the performance of HfO_2-based pyroelectrics. Indeed, in pyroelectric measurements, the pyroelectric thin film rigidly attached to a thick substrate is free to expand only in the thickness dimension [55]. The thermal expansion mismatch between the film (α_1^{film}) and the substrate (α_1^{sub}) causes an extrinsic (in the basal plane the thermal
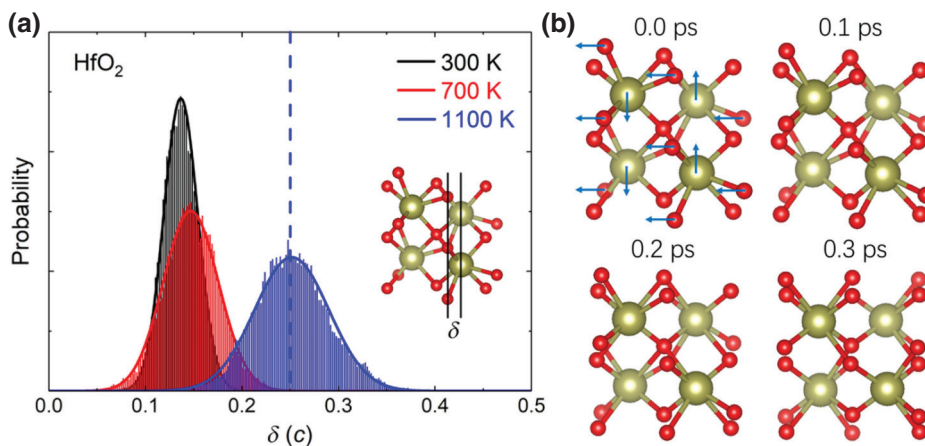

FIG. 4. (a) Probability distribution of the atomic displacement for *NPT* simulations at selected temperatures. The atomic displacement, δ, is the relative distance between the O and Hf planes in the polar direction, which is defined as a fraction of the lattice constant c ($\delta = 0.25$ corresponds to the tetragonal phase). (b) The instantaneous unit-cell structures (projected from supercell structures) at selected time frames during the phase transition for the *NPT* simulation at 900 K.
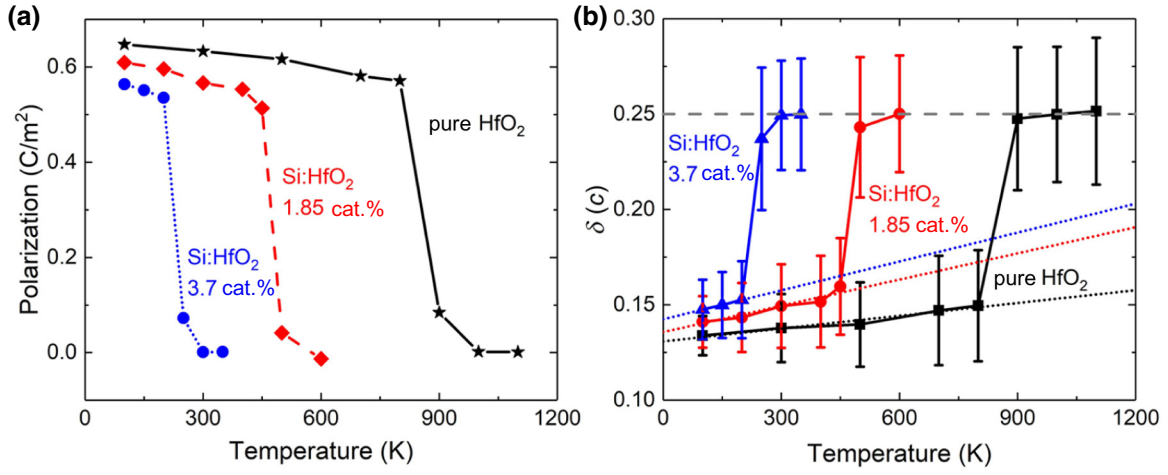
FIG. 5. For pure and Si-doped HfO_2: (a) Pyroelectric response calculated with AIMD simulations. Si-doped HfO_2 is modeled by substituting 2 (1.85 cat.%) and 4 (3.7 cat.%) Hf atoms with Si atoms in a supercell of 324 atoms. (b) Temperature-dependent atomic displacement δ [see Fig. 4(a) for definition]. The dotted lines represent the notable atomic displacement introduced by the incorporation of Si dopants.

expansion of the film is subject to that of the substrate) pyroelectric effect via the piezoelectricity of the film (d_{31}). To determine such an impact, a wide-frequency-range method has been demonstrated in pyroelectric measurements [56,57]. In the literature [56,57], at low frequencies, the film expands in plane with the substrate, while at high frequencies the film is clamped to the substrate at constant temperature. The effective low- (Eq. 9 in Ref. [55]) and high-frequency (Eq. 8 in Ref. [55]) pyroelectric coefficients are [56] (s is the elastic compliance constant)

$$\Pi^{\mathrm{low}} = \Pi - \frac{2d_{31}(\alpha_1^{\mathrm{film}} - \alpha_1^{\mathrm{sub}})}{s_{11} + s_{12}}, \qquad (5)$$

$$\Pi^{\mathrm{high}} = \Pi - \frac{2d_{31}\alpha_1^{\mathrm{film}}}{s_{11} + s_{12}}. \qquad (6)$$

The difference, $2d_{31}\alpha_1^{\mathrm{sub}}/(s_{11} + s_{12})$, yields the coupling between the piezoelectricity of the film and the in-plane thermal expansion of the substrate [56]. This term, which is also referred to as the "secondary" pyroelectricity in some pyroelectric measurements [56–58], needs to be distinguished from the intrinsic Π_2.

Last, but not least, for the purpose of characterizing and enhancing the pyroelectric response utilizing HfO_2-based pyroelectrics in applications, some important implications can be made. Mart *et al.* [58] used the wide-frequency-range method to characterize the pyroelectric response of Si-doped HfO_2, and obtained the extrinsic secondary pyroelectric coefficient ($\Pi^{\mathrm{low}} - \Pi^{\mathrm{high}}$) of $-19\ \mu\mathrm{C}/(\mathrm{m}^2\ \mathrm{K})$, which is comparable to the calculated intrinsic Π_2 of $-29\ \mu\mathrm{C}/(\mathrm{m}^2\ \mathrm{K})$ for pure HfO_2. This highlights the "secondary" contribution from the in-plane thermal expansion of the substrate. Noting that d_{31} is typically negative, a direct comparison of the thermal expansion coefficients of

the film (calculated, $\alpha_1^{\mathrm{film}} \approx 5.6 \times 10^{-6}/K$) and the substrate (e.g., using TiN as top and bottom electrodes [17,19, 20,58], measured [59], $\alpha_1^{\mathrm{sub}} \approx 9.9 \times 10^{-6}/K$) indicates that Π^{low} and Π^{high} are negative (overestimating Π) and positive (underestimating Π), respectively. This partly explains the fact that our theoretical Π for pure HfO_2 is smaller in magnitude than that of low-frequency measurements for Si-doped HfO_2 [19,20,58]. In low-frequency pyroelectric applications, the pyroelectric response can be further enhanced by depositing thin-film HfO_2 on substrates with much larger coefficients of thermal expansion [41].

As for Si-doped HfO_2, Π (mainly Π_1) becomes larger in magnitude with increasing doping concentration, as a result of reduced transition temperature; this suggests that Si doping not only promotes stabilization, but also enhances the primary pyroelectric response. We have attributed the enhanced primary pyroelectricity to the perturbation of local chemical environment due to Si doping. Considering that Si and Hf ions are equivalent, one can expect that the incorporation of other dopants (e.g., divalent dopants, such as Sr; trivalent dopants, such as Y; and four-valent dopants, such as Ce) may further enhance the pyroelectric response. In fact, these dopants have been revealed as promising candidates to promote ferroelectricity in HfO_2 [15,16]. The effect of these dopants on pyroelectricity will be discussed in a future work.

VI. CONCLUSIONS

In summary, we have applied a first-principles lattice-dynamics approach to identify the underlying mechanisms responsible for pyroelectricity in the recently discovered ferroelectric phase of HfO_2. Unlike most conventional ferroelectric pyroelectrics, the secondary pyroelectricity

dominates in the $Pca2_1$ orthorhombic phase of pure HfO$_2$, due to an unusual negative longitudinal piezoelectricity together with an isotropic positive thermal expansion. We further demonstrate with AIMD simulations that the secondary effect is associated with an orthorhombic (polar) to tetragonal (nonpolar) structural phase transition. The phase transition occurs at around 850 K and is identified to be displacive. With the incorporation of Si dopants, such phase transition persists, but occurs at reduced temperatures. Si doping perturbs the host HfO$_2$ structure, introducing strong anharmonicity, and hence, the primary pyroelectric response is enhanced. The present work unravels and highlights the secondary pyroelectric effect that is responsible for the pyroelectricity in HfO$_2$ and provides important implications for practical applications utilizing HfO$_2$-based pyroelectrics. In pursuit of an enhanced pyroelectric response, substrates that exhibit large thermal expansion and dopants that strongly perturb the host HfO$_2$ structure are desired.

[1] D. Damjanovic, Ferroelectric, dielectric and piezoelectric properties of ferroelectric thin films and ceramics, Rep. Prog. Phys. **61**, 1267 (1998).

[2] S. B. Lang, Pyroelectricity: From ancient curiosity to modern imaging tool, Phys. Today **58**, 31 (2005).

[3] R. W. Whatmore, Pyroelectric devices and materials, Rep. Prog. Phys. **49**, 1335 (1986).

[4] Y. Yang, S. Wang, Y. Zhang, and Z. L. Wang, Pyroelectric nanogenerators for driving wireless sensors, Nano Lett. **12**, 6408 (2012).

[5] Y. Yang, W. Guo, K. C. Pradel, G. Zhu, Y. Zhou, Y. Zhang, Y. Hu, L. Lin, and Z. L. Wang, Pyroelectric nanogenerators for harvesting thermoelectric energy, Nano Lett. **12**, 2833 (2012).

[6] J. Liu and S. T. Pantelides, Mechanisms of Pyroelectricity in Three- and Two-Dimensional Materials, Phys. Rev. Lett. **120**, 207602 (2018).

[7] J. Liu and S. T. Pantelides, Anisotropic thermal expansion of group-IV monochalcogenide monolayers, Appl. Phys. Express **11**, 101301 (2018).

[8] M. Mehboudi, B. M. Fregoso, Y. Yang, W. Zhu, A. van der Zande, J. Ferrer, L. Bellaiche, P. Kumar, and S. Barraza-Lopez, Structural Phase Transition and Material Properties of Few-Layer Monochalcogenides, Phys. Rev. Lett. **117**, 246802 (2016).

[9] S. Barraza-Lopez, T. P. Kaloni, S. P. Poudel, and P. Kumar, Tuning the ferroelectric-to-paraelectric transition temperature and dipole orientation of group-IV monochalcogenide monolayers, Phys. Rev. B **97**, 024110 (2018).

[10] T. Böscke, J. Müller, D. Bräuhaus, U. Schröder, and U. Böttger, Ferroelectricity in hafnium oxide thin films, Appl. Phys. Lett. **99**, 102903 (2011).

[11] J. Müller, T. S. Böscke, U. Schröder, S. Mueller, D. Bräuhaus, U. Böttger, L. Frey, and T. Mikolajick, Ferroelectricity in simple binary ZrO$_2$ and HfO$_2$, Nano Lett. **12**, 4318 (2012).

[12] M. Hoffmann, U. Schroeder, C. Künneth, A. Kersch, S. Starschich, U. Böttger, and T. Mikolajick, Ferroelectric phase transitions in nanoscale HfO$_2$ films enable giant pyroelectric energy conversion and highly efficient supercapacitors, Nano Energy **18**, 154 (2015).

[13] M. H. Park, Y. H. Lee, H. J. Kim, Y. J. Kim, T. Moon, K. D. Kim, J. Müller, A. Kersch, U. Schroeder, and T. Mikolajick, Ferroelectricity and antiferroelectricity of doped thin HfO$_2$-based films, Adv. Mater. **27**, 1811 (2015).

[14] M. H. Park, H. J. Kim, Y. J. Kim, T. Moon, K. D. Kim, and C. S. Hwang, Toward a multifunctional monolithic device based on pyroelectricity and the electrocaloric effect of thin antiferroelectric Hf$_x$Zr$_{1-x}$O$_2$ films, Nano Energy **12**, 131 (2015).

[15] R. Batra, T. D. Huan, G. A. Rossetti, Jr., and R. Ramprasad, Dopants promoting ferroelectricity in hafnia: Insights from a comprehensive chemical space exploration, Chem. Mater. **29**, 9102 (2017).

[16] C. Künneth, R. Materlik, M. Falkowski, and A. Kersch, Impact of four-valent doping on the crystallographic phase formation for ferroelectric HfO$_2$ from first-principles: Implications for ferroelectric memory and energy-related applications, ACS Appl. Nano Mater. **1**, 254 (2018).

[17] M. H. Park, C. C. Chung, T. Schenk, C. Richter, M. Hoffmann, S. Wirth, J. L. Jones, T. Mikolajick, and U. Schroeder, Origin of temperature-dependent ferroelectricity in Si-doped HfO$_2$, Adv. Electron. Mater. **4**, 1700489 (2018).

[18] S. Smith, A. Kitahara, M. Rodriguez, M. Henry, M. Brumbach, and J. Ihlefeld, Pyroelectric response in crystalline hafnium zirconium oxide (Hf$_{1-x}$Zr$_x$O$_2$) thin films, Appl. Phys. Lett. **110**, 072901 (2017).

[19] S. Jachalke, T. Schenk, M. H. Park, U. Schroeder, T. Mikolajick, H. Stöcker, E. Mehner, and D. C. Meyer, Pyroelectricity of silicon-doped hafnium oxide thin films, Appl. Phys. Lett. **112**, 142901 (2018).

[20] C. Mart, T. Kämpfe, S. Zybell, and W. Weinreich, Layer thickness scaling and wake-up effect of pyroelectric

response in Si-doped HfO$_2$, Appl. Phys. Lett. **112,** 052905 (2018).

[21] S. Pandya, G. Velarde, L. Zhang, and L. W. Martin, Pyroelectric and electrocaloric effects in ferroelectric silicondoped hafnium oxide thin films, Phys. Rev. Mater. **2,** 124405 (2018).

[22] R. Resta, Electrical polarization and orbital magnetization: The modern theories, J. Phys. Condens. Matter **22,** 123201 (2010).

[23] B. Szigeti, Temperature Dependence of Pyroelectricity, Phys. Rev. Lett. **35,** 1532 (1975).

[24] M. Born, On the quantum theory of pyroelectricity, Rev. Mod. Phys. **17,** 245 (1945).

[25] F. Bernardini, V. Fiorentini, and D. Vanderbilt, Spontaneous polarization and piezoelectric constants of III-V nitrides, Phys. Rev. B **56,** R10024 (1997).

[26] A. Belabbes, J. Furthmüller, and F. Bechstedt, Relation between spontaneous polarization and crystal field from first principles, Phys. Rev. B **87,** 035305 (2013).

[27] Q. Peng and R. E. Cohen, Origin of pyroelectricity in LiNbO$_3$, Phys. Rev. B **83,** 220103 (2011).

[28] J. Liu, M. V. Fernández-Serra, and P. B. Allen, Firstprinciples study of pyroelectricity in GaN and ZnO, Phys. Rev. B **93,** 081205 (2016).

[29] N. Mounet and N. Marzari, First-principles determination of the structural, vibrational and thermodynamic properties of diamond, graphite, and derivatives, Phys. Rev. B **71,** 205214 (2005).

[30] P. Giannozzi et al., QUANTUM ESPRESSO: A modular and open-source software project for quantum simulations of materials, J. Phys.: Condens. Matter **21,** 395502 (2009).

[31] R. King-Smith and D. Vanderbilt, Theory of polarization of crystalline solids, Phys. Rev. B **47,** 1651 (1993).

[32] R. Resta and D. Vanderbilt, in *Physics of Ferroelectrics: A Modern Perspective*, edited by C. Ahn and K. M. Rabe (Springer-Verlag, Berlin, 2007), Vol. 105, p. 31.

[33] R. Resta, M. Posternak, and A. Baldereschi, Towards a Quantum Theory of Polarization in Ferroelectrics: The Case of KNbO$_3$, Phys. Rev. Lett. **70,** 1010 (1993).

[34] D. M. Ceperley and B. Alder, Ground State of the Electron Gas by a Stochastic Method, Phys. Rev. Lett. **45,** 566 (1980).

[35] J. P. Perdew and A. Zunger, Self-interaction correction to density-functional approximations for many-electron systems, Phys. Rev. B **23,** 5048 (1981).

[36] A. Dal Corso, Pseudopotentials periodic table: From H to Pu, Comput. Mater. Sci. **95,** 337 (2014).

[37] K. Momma and F. Izumi, VESTA 3 for three-dimensional visualization of crystal, volumetric and morphology data, J. Appl. Crystallogr. **44,** 1272 (2011).

[38] J. M. Soler, E. Artacho, J. D. Gale, A. García, J. Junquera, P. Ordejón, and D. Sánchez-Portal, The SIESTA method for ab initio order-N materials simulation, J. Phys.: Condens. Matter **14,** 2745 (2002).

[39] S. Nosé, A unified formulation of the constant temperature molecular dynamics methods, J. Chem. Phys. **81,** 511 (1984).

[40] M. Parrinello and A. Rahman, Polymorphic transitions in single crystals: A new molecular dynamics method, J. Appl. Phys. **52,** 7182 (1981).

[41] B. Hanrahan, Y. Espinal, C. Neville, R. Rudy, M. Rivas, A. Smith, M. Kesim, and S. Alpay, Accounting for the various contributions to pyroelectricity in lead zirconate titanate thin films, J. Appl. Phys. **123,** 124104 (2018).

[42] B. Hanrahan, Y. Espinal, S. Liu, Z. Zhang, A. Khaligh, A. Smith, and S. P. Alpay, Combining inverse and conventional pyroelectricity in antiferroelectric thin films for energy conversion, J. Mater. Chem. C **6,** 9828 (2018).

[43] T. D. Huan, V. Sharma, G. A. Rossetti, Jr., and R. Ramprasad, Pathways towards ferroelectricity in hafnia, Phys. Rev. B **90,** 064111 (2014).

[44] R. Batra, T. D. Huan, J. L. Jones, G. Rossetti, Jr., and R. Ramprasad, Factors favoring ferroelectricity in hafnia: A first-principles computational study, J. Phys. Chem. C **121,** 4139 (2017).

[45] M. H. Park, T. Schenk, C. M. Fancher, E. D. Grimley, C. Zhou, C. Richter, J. M. LeBeau, J. L. Jones, T. Mikolajick, and U. Schroeder, A comprehensive study on the structural evolution of HfO$_2$ thin films doped with various dopants, J. Mater. Chem. C **5,** 4677 (2017).

[46] S. Clima, D. Wouters, C. Adelmann, T. Schenk, U. Schroeder, M. Jurczak, and G. Pourtois, Identification of the ferroelectric switching process and dopant-dependent switching properties in orthorhombic HfO$_2$: A first principles insight, Appl. Phys. Lett. **104,** 092906 (2014).

[47] X. Sang, E. D. Grimley, T. Schenk, U. Schroeder, and J. M. LeBeau, On the structural origins of ferroelectricity in HfO$_2$ thin films, Appl. Phys. Lett. **106,** 162905 (2015).

[48] R. Materlik, C. Künneth, and A. Kersch, The origin of ferroelectricity in Hf$_{1-x}$Zr$_x$O$_2$: A computational investigation and a surface energy model, J. Appl. Phys. **117,** 134109 (2015).

[49] P. Polakowski and J. Müller, Ferroelectricity in undoped hafnium oxide, Appl. Phys. Lett. **106,** 232905 (2015).

[50] G. Sághi-Szabó, R. E. Cohen, and H. Krakauer, FirstPrinciples Study of Piezoelectricity in PbTiO$_3$, Phys. Rev. Lett. **80,** 4321 (1998).

[51] I. Katsouras, K. Asadi, M. Li, T. B. Van Driel, K. S. Kjaer, D. Zhao, T. Lenz, Y. Gu, P. W. Blom, and D. Damjanovic, The negative piezoelectric effect of the ferroelectric polymer poly(vinylidene fluoride), Nat. Mater. **15,** 78 (2016).

[52] S. Liu and R. Cohen, Origin of Negative Longitudinal Piezoelectric Effect, Phys. Rev. Lett. **119,** 207601 (2017).

[53] See Supplemental Material at http://link.aps.org/supplemental/10.1103/PhysRevApplied.12.034032 for additional data on rigid-ion primary pyroelectricity of pure HfO$_2$, AIMD simulations with the PBE functional for pure HfO$_2$, the anharmonic potential energy of Si:HfO$_2$, and the thermal expansion and piezoelectricity of Si:HfO$_2$.

[54] J. P. Perdew, K. Burke, and M. Ernzerhof, Generalized Gradient Approximation Made Simple, Phys. Rev. Lett. **77,** 3865 (1996).

[55] J. Zook and S. Liu, Pyroelectric effects in thin film, J. Appl. Phys. **49,** 4604 (1978).

[56] T. Tong, J. Karthik, L. W. Martin, and D. G. Cahill, Secondary effects in wide frequency range measurements of the pyroelectric coefficient of Ba$_{0.6}$Sr$_{0.4}$TiO$_3$ and PbZr$_{0.2}$Ti$_{0.8}$O$_3$ epitaxial layers, Phys. Rev. B **90,** 155423 (2014).

[57] S. Pandya, J. D. Wilbur, B. Bhatia, A. R. Damodaran, C. Monachon, A. Dasgupta, W. P. King, C. Dames, and L. W. Martin, Direct Measurement of Pyroelectric and Electrocaloric Effects in Thin Films, Phys. Rev. Appl. **7,** 034025 (2017).

[58] C. Mart, M. Czernohorsky, S. Zybell, T. Kämpfe, and W. Weinreich, Frequency domain analysis of pyroelectric response in silicon-doped hafnium oxide (HfO_2) thin films, Appl. Phys. Lett. **113,** 122901 (2018).

[59] K. Aigner, W. Lengauer, D. Rafaja, and P. Ettmayer, Lattice parameters and thermal expansion of $Ti(C_xN_{1-x})$, $Zr(C_xN_{1-x})$, $Hf(C_xN_{1-x})$ and TiN_{1-x} from 298 to 1473 K as investigated by high-temperature X-ray diffraction, J. Alloys Compd. **215,** 121 (1994).